Nanoscale

Accepted Manuscript

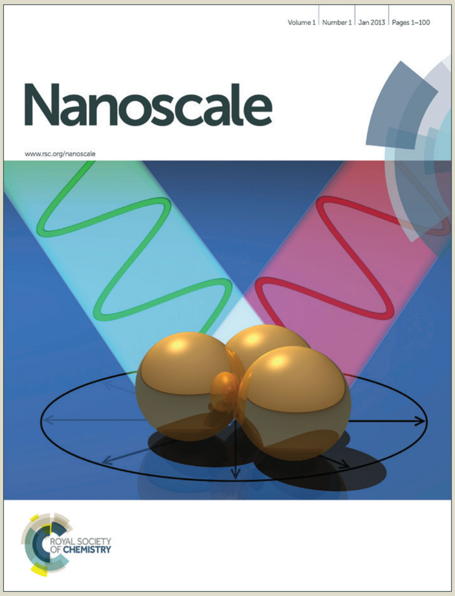

ROYAL SOCIETY OF CHEMISTRY

www.rsc.org/nanoscale

Decrease in Thermal Conductivity in Polymeric P3HT Nanowires by Size-Reduction induced by Crystal Orientation: New Approaches towards Organic Thermal Transport Engineering.

Miguel Muñoz Rojo[1], *Jaime Martín*[1], *Stèphane Grauby*[2], *Theodorian Borca-Tasciuc*[3], *Stefan Dilhaire*[2] *and Marisol Martin-Gonzalez*[1].

[1] Instituto de Microelectrónica de Madrid, Calle de Isaac Newton, 8 28760 Tres Cantos, Madrid, Spain.
[2] Univ. Bordeaux, LOMA, UMR 5798, 33405 Talence, France.
[3] Rensselaer Polytechnique Institute, 110 8th St, Troy, NY 12180, United States.

Abstract

To date, there is no experimental characterization of thermal conductivity of semiconductor polymeric individual nanowires embedded in a matrix. This work reports on Scanning Thermal Microscopy measurements in 3ω configuration to determine how the thermal conductivity of individual nanowires made of a model conjugated polymer (P3HT) is modified when decreasing their diameters. We observe a reduction of the thermal conductivity, from λ_{NW}=2.29±0.15W/K·m to λ_{NW}=0.5±0.24W/K·m, when the diameter of nanowires is reduced from 350 nm to 120 nm, which correlates with the polymer crystal orientation measured by WAXS. Through this work, the foundations for future polymer thermal transport engineering are presented.

Keywords: 3ω-Scanning Thermal Microscopy, Organic P3HT Nanowires, size-confinement effects, thermal conductivity reduction.

Nanostructuring is used to modify and control the transport properties of materials due to confinement effects. For example, thermal conductivity reduction by size effects has yielded to more efficient thermoelectric devices[1] [2]. Among transport properties of materials, especially challenging are measurements of the thermal conductivity, that become even more difficult as the dimension of the material is reduced [3]. However, the analysis of this physical property under nanoscale confinement is mandatory for a wide variety of technological applications ranging from thermoelectrics to nanoscopic thermal insulation, among others.

Generally, size effects on the thermal transport properties are dramatic for 1D nanostructures due mainly to scattering processes, as heat propagation is confined to a single spatial dimension. This has been theoretically predicted and experimentally observed for inorganic nanowires (NWs) [3, 4]. However, little is known about how low dimensionality affects the thermal transport properties in semiconducting polymer materials, although severe changes are also expected, because nanoconfinement is well known to induce structural and dynamical changes in nanoconfined polymers [5].

Thereby, our aim is to clarify how the thermal conductivity of relevant semiconducting polymer nanowires inside a matrix is altered by nanoconfinement.

Shen et al. [6] measured for the first time the thermal conductivity of single ultra-drawn polyethylene (PE) NWs and observed a dramatic increase of the thermal conductivity of the NW as reducing diameter, which was correlated to the molecular orientation and reduction of voids and defects. Likewise, Cao et al. [7] reported the enhancement of thermal conductivity of PE NWs. However, the measured NWs consisted of collapsed bundles of NWs and thus, these measurement might be influenced by the different environments experienced by the NWs-NWs at interior positions of the bunch, from those at external positions, free NWs, etc. Therefore, to understand the thermal behavior of NWs it is mandatory to study the thermal transport of isolated NW in well controlled boundary conditions. For our study, we have selected poly(3-hexylthiophene) (P3HT) as model semiconducting polymer, as P3HT is one of the best characterized semiconducting polymers from a structural point of view [8]. Furthermore, it has recently shown promising thermoelectric figures of merit at room temperature, for which the characterization of the thermal conductivity was crucial to calculate its efficiency [9]. Although little is known on the confinement effects on thermal properties of P3HT, the few works reported on P3HT 2D thin films have shown anisotropy of the thermal conductivity along the different spatial dimensions[10] [11]. However, measurements of individual NW are extremely challenging due to the high spatial resolution required and only very few techniques are able to do it with accuracy [3].

In this work, a technique called 3ω-SThM and based on Scanning Probe Microscopy (SPM)[12] has been used to carry out the first local measurements of thermal conductivity on individual semiconducting polymer NWs. These measurements fill a gap in literature and constitute a step toward the determination of how polymer materials behave at this low scale.

On the one hand, the most typical technique that is able to measure the thermal conductivity of single NWs is the microfabricated suspended device technique [13]. Nevertheless, it is worth mentioning that this method, which measures only one NW at the same time, requires many heavy processing steps and may leads to the oxidation of the surface of the NWs, since they are not embedded in a matrix but in contact with air.

In addition, this technique measures the thermal conductivity of one NW isolated from its matrix which can differ from the thermal conductivity of the NWs embedded in the matrix, which constitutes the effective functioning device, because of the matrix/NWs interactions [14] . On the other hand, there are several techniques that can carry out local thermal characterization of arrays of nanowires embedded in a matrix, such as the time domain thermoreflectance (TDTR) [14] , the photoacoustic technique [15], photo-thermoelectric technique [16] or others based on micro-probe measurements[17]. Nevertheless, the typical spatial resolution reached by these technique are about 1µm, which do not enable them to carry out thermal measurements on individual nanowires but they give access to a mean value of the thermal conductivity of the whole sample. The 3ω-SThM is a local technique that enables to carry out thermal images of individual NWs with a 100nm typical thermal spatial resolution and a 10nm typical topographical spatial resolution. This technique has the advantage to probe thermally a wide range of individual NWs embedded in their matrix in short periods of time, ranging from 10 to 20 min depending on the signal generator frequency used[18] [19] [20] . We obtain at the same time a topographical image and a thermal image, enabling an easy localization of the NWs. Determining at the same time if the pore is filled, what is the morphological quality of the nanowires studied, etc. In addition from a single thermal image, we can assess as many NWs measurements as the number of NWs in the image, leading to a mean value and a standard deviation of the measured signal among nanowires [21].

Thermal conductivity measurements are carried out with a 3ω-SThM (Scanning Thermal Microcopy) working in contact mode (see supporting information S2). This technique has been recently used to measure the thermal conductivity of inorganic NWs of Si [19] , SiGe[21] or Bi_2Te_3[20]. Classically, 3ω-SThM measurements are performed using a Wollastone probe [22]. However, the Wollastone probes face two main drawbacks: a thermal spatial resolution around 1µm comparable to TDTR, which makes it unsuitable to probe individual NWs measurements at nanometric scale, and a low thermal cut-off frequency which infers a low excitation frequency and hence a high acquisition time. Pd/SiO_2 probes used in our measurements present a 100nm thermal spatial resolution and a cut-off frequency ten times higher than the Wollastone one [18]. Thereby, in this work the thermal conductivity of individual P3HT NW (with diameters of 120 nm, 220 nm and 350 nm) have been assessed by the Scanning Thermal Microscopy working in 3ω configuration while embedded in the alumina template.

The hexagonally ordered AAO templates with pores of 120, 220, and 350 nm in diameter and 100 µm in length were synthesized by a two-step electrochemical anodization of aluminum and subsequent chemical etching as reported in the literature for templates with pore diameter in the 120-400 nm range [23] [24] (Supporting Information Figure S1). For the fabrication of P3HT NWs, macroscopic pieces of commercial P3HT from Aldrich Ltd. (M_n=33 405 g/mol, M_w/M_n=1.50, regionregularity = 96%) were placed onto the surface of the AAO at 260 °C for 45 min in N_2 atmosphere[25]. Then the samples were taken out from the furnace, and quenched in ice-water, so that P3HT rapidly solidified. The excess of P3HT at the AAO top surfaces was removed with a razor blade and the surface polished with diamond paste (3 µm, Buehler MetaDi II). SEM micrographs of the surface of infiltrated templates are shown in the supporting information Figure S1a and S1b. Finally, the P3HT-infiltrated templates were annealed at 125 °C for 30 min. A sketch of the samples is included in the Supporting Information Figure S1c.

Wide-angle X-ray scattering (WAXS) experiments in a geometry in which the wave vector, *Q,* was parallel to the long axis of P3HT NWs were carried out in reflection geometry using a Philips X'Pert diffractometer, (supporting information Figure S3a). Moreover, WAXS experiments were also carried out in transmission geometry with the X-ray beam traveling along the direction perpendicular to the template surface using a Bruker AXS Nanostar X-ray scattering instrument (see Supplementary Information Figure S3b), so that *Q* was nearly perpendicular to the long axis of NWs. The underlying Al substrate was chemically etched from the AAO templates for transmission measurements. The scattered X-rays were detected using a two dimensional multiwire area detector (Bruker Hi-Star). The data were then converted to one-dimensional scattering profiles by radial averaging along the azimuthal direction. The sample to detector distance was 10 cm. Both instruments use Cu K_α radiation (1.54 Å).

The 3ω-SThM was applied to measure P3HT NWs with different diameters embedded in a porous alumina matrix. It is important mentioning that this experimental technique not only allows measurements of the thermal resistance, R_{eq}, of individual NW inside the matrix, but it also gives information of the R_{eq} of the whole composite[20] . This technique is based on a statistical data processing to determine the mean average of the equivalent thermal resistance of the NWs and the whole composite, with its associated standard deviation.

Figure 1a shows Scanning Electron Microscopy (SEM) pictures of a top view of the un-filled porous alumina templates used to embed P3HT NW, as well as topographic (Figure 1b) and 3ω voltage ($(V_{3\omega})_{Tip}$) (Figure 1c) images of P3HT NWs with three different nanowire diameters size, 350nm, 220nm and 120nm, respectively. Additional SEM images of the P3HT NW embedded in the template are shown in the supporting information Figure S1a and S1b.

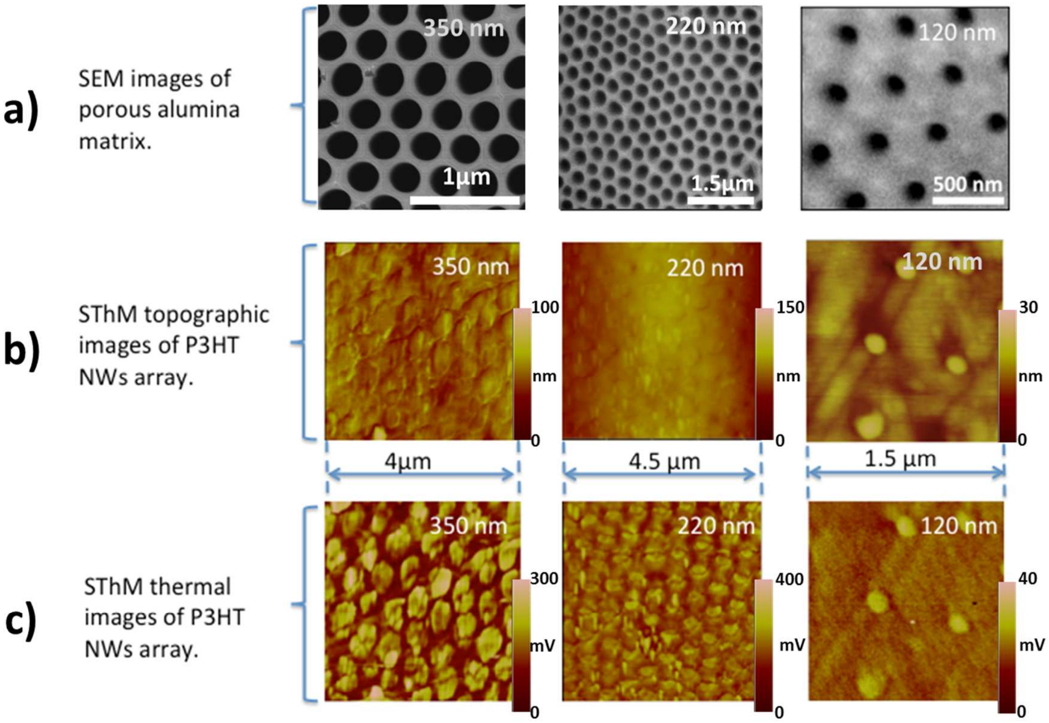

Figure 1.a) SEM pictures of the three different diameter size porous alumina matrix used to embedded P3HT NWs, b) topographic of the filled templates and c) $(V_{3\omega})_{Tip}$ or thermal images of P3HT NWs taken with a 3ω-SThM.

According to the $(V_{3\omega})_{Tip}$ thermal images of P3HT NWs, we can distinguish two areas in each of them: a high $V_{3\omega}$ signal area corresponding with the NWs locations and a low $V_{3\omega}$ signal area on the alumina. Then, the NW mean equivalent thermal resistances $(R_{eq})_{NW}$ for the three different diameters can be determined from the $V_{3\omega}$ value measured on each NW. The results are shown in Table I. Let us underline that each $(R_{eq})_{NW}$ value presented in this table has been obtained after measurements on 20NWs (even for the 120nm NW sample for which we have used a thermal image larger than the one in Figure 1c). In this table it is also included the thermal exchange radius of the tip r_{ex}, whose value was specifically measured before each sample scan. It constitutes an important parameter to take into account when doing this analysis (Supporting Information S2). Indeed, not only does it influence the spatial resolution but it is also a key parameter in the estimation of the thermal conductivity through the evaluation of some of the thermal resistances involved in the total equivalent thermal resistance measured, as developed below [18].

After the evaluation of the equivalent thermal resistance $(R_{eq})_{NW}$ on the NWs, one can determine the thermal conductivity of the NW. For that purpose, one must consider that the equivalent thermal resistance measured can generally be expressed as the addition of 4 thermal resistances in series, the tip to sample contact thermal resistance R_C, the constriction resistance $R_{tip\text{-}NW}$ of the heat flux between the tip and the NW, the sample intrinsic thermal resistance R_{Com}, and the constriction resistance $R_{NW\text{-}Sub}$ of the heat flux between the NW and the substrate on which the composite is deposited [20]. This is expressed by equation (1),

$$(R_{eq})_{NW} = R_{Tip-NW} + R_C + R_{Com} + R_{NW-Sub} \tag{1}$$

On the one hand, the constriction resistance between the tip and the NW, $R_{Tip\text{-}NW}$, is negligible as the thermal exchange surface is larger than the NW section, whose diameters vary from 350 nm to 120 nm. On the other hand, the heat flows through the whole composite and, given that the matrix is 100µm thick, the majority of the heat will not reach the substrate. Therefore, the constriction resistance between the NW and the substrate can be neglected.

Therefore, equation (1) is reduced to,

$$(R_{eq})_{NW} = R_C + R_{Com} \tag{2}$$

In order to determine R_{Com} and subsequently λ_{Com}, it is now necessary to evaluate the thermal contact resistance, R_C. As developed by Lefevre et al.[22] , this resistance takes into account not only the solid-solid conduction between tip and sample, but also conduction through air and through the water meniscus, which constitutes the two other main heat transfer mechanisms under atmospheric conditions. It can be expressed as:

$1/R_C = G_c = G_S + G_A + G_W$ where G_S, G_A and G_W are respectively the conductance through solid-solid contact, through the air and through the water meniscus. The heat transfer mechanisms take place over a surface not defined by the contact-contact radius but by the thermal exchange radius r_{ex}, hence the necessity to calibrate this parameter [18].

To evaluate R_C we measure the equivalent thermal resistance on the alumina matrix [19, 20, 26, 27]. Indeed, in this case, the equivalent thermal resistance measured on the alumina is given by:

$$\left(R_{eq}\right)_{Alu} = R_c + R_{Tip-Alu} \tag{3}$$

where $R_{Tip-Alu}$ is the constriction resistance between the tip and the alumina matrix. Considering the matrix as a semi-infinite medium due to its dimensions in comparison with the thermal exchange radius r_{ex}, the constriction resistance can be expressed as [27] $R_{Tip-Alu} = \frac{1}{4\lambda_{Alu} r_{ex}}$ where λ_{Alu} is the thermal conductivity of the alumina.

As it was commented in ref.[20], the intrinsic thermal resistance R_{Com} does not correspond to the NW intrinsic thermal resistance, but to the local composite (alumina and NW) thermal resistance. Indeed, first, the thermal exchange surface is larger than the NW section; hence the hot tip heats not only the NW but the surrounding alumina matrix at the same time. In addition, the heat passing through the NW spreads towards the matrix since the NWs are in contact with the alumina and NWs and alumina are not expected to have much different thermal conductivities. R_{Com} can then be expressed as a constriction resistance on a semi-infinite effective medium,

$$R_{Com} = \frac{1}{4\lambda_{Com} r_{ex}} \tag{4}$$

where λ_{Com} is the thermal conductivity of the composite calculated using the effective medium theory [14 20]:

$$\lambda_{Com} = x\lambda_{NW} + (1-x)\lambda_{Alu} \tag{5}$$

where x is the areal packing density of the NW array, λ_{NW} and λ_{Alu} the intrinsic NW and the porous alumina matrix thermal conductivities, respectively. In ref. [14], the authors study in detail the validity of two models to describe the thermal exchanges between NWs and matrix, namely the effective medium and two-temperature models, when heating a sample made of NWs in a matrix using a modulated heart source. It is demonstrated that when the heat source is modulated at low frequencies ($f<1MHz$), which is our case ($f=1kHz$), the measured thermal conductivity approaches the thermal conductivity predicted by effective medium theory (equation (5)) with a thermal conductance of the matrix/NW $_{\text{interfaces}}$ $G_{\text{matrix}}/\text{NW} \rightarrow \infty$. Then, NWs and matrix are strongly coupled and the heat passing from the tip to the NW spreads to the surrounding matrix. We hence heat the whole composite medium over the thermal penetration length, which are typically several microns at this low frequency.

Table I. Areal packing density of the NW array and alumina, thermal exchange radius, equivalent thermal resistance and thermal conductivities of the composite, alumina matrix and intrinsic NWs for three different composites made of P3HT NWs array embedded in alumina matrix.

Nanowire diameters (nm)	Packing areal density of the NW array	Thermal exchange radius (nm)	$(R_{eq})_{NW}$ (K/W) $\times 10^6$	$(R_{eq})_{Alumina}$ (K/W) $\times 10^6$	Composite thermal conductivity (W/K·m)	Alumina matrix thermal conductivity (W/K·m)	NW thermal conductivity (W/Km)
350	0.55	175±10	4.36±0.11	4.63±0.03	1.89±0.08	1.38	2.29±0.15
220	0.25	175±10	4.49±0.06	4.34±0.02	1.18±0.06	1.38	0.70±0.12
120	0.08	81±5	6.48±0.03	6.36±0.02	1.31±0.02	1.38	0.50±0.24

Then, from the same $(V_{3\omega})_{Tip}$ image presented in Figure 1c we measured the $(V_{3\omega})_{Tip}$ signal on 20 locations on the alumina area for the three samples with porous size of 350nm, 220nm and 120nm. The thermal conductivity of the alumina matrix resulted to be λ_{Alu}=1.38W/K·m, see Table I, for the three templates. The thermal conductivity values show consistence since all the templates were prepared under the same conditions; [23] [25] the only difference is that the pores are widening by chemical etching and the porosity increase. With these values of the alumina the mean contact resistances are determined to be, $R_C=3.60\times10^6$ K/W, $R_C=3.31\times10^6$ K/W and $R_C=4.12\times10^6$ K/W for the alumina with 350 nm, 220 nm and 120 nm in diameter pores, respectively. Often, the contact resistance is determined by calibration on a material of known thermal conductivity [26] [17]. It is then assumed that Rc does not change from sample to sample and when measuring other materials. Nevertheless, precautions need to be taken since this contact resistance may be very dependent on various parameters such as the surface roughness or the tip-to-sample contact geometry. In our case, when measuring $(R_{eq})_{Alumina}$ on the alumina part of the three samples, even if the tip is identical, we measure three different values (Table I), hence three different contact resistances. We have previously proposed[19] an original method to determine *Rc* accurately: from a 3ω-SThM image, we deduce it from the equivalent thermal resistances measured directly on the NWs. This method demands a sample with NWs offering wide diameter dispersion, which is not the case here. But we have also shown[19] that, determining the mean contact resistance subsequently from the equivalent thermal resistance measured from the same 3ω-SThM image on the matrix of the same sample, the estimated values obtained by both methods differ by less than 1%. Therefore, if it does not seem appropriate to evaluate the contact resistance on a given sample and then use the same value for other samples, measuring R_c on a part of a sample seems to give a reliable value that can be used on another part of the same sample from a thermal image obtained during the same scan under the same experimental conditions, in particular with a contact force between tip and sample maintained constant by the AFM feedback loop.

Afterwards, we take into account a possible ±1% relative error in the contact resistance. This value, which is also consistent with the standard deviation evaluated on $(R_{eq})_{Alumina}$ in Table I and from which we deduce R_c, can appear small in comparison with classical mechanical contact resistance relative variations. Indeed, it only takes into account the repeatability error which is reduced because, from one image, we do 20 measurements on the alumina part, reducing the standard deviation by almost 5. With this ±1% possible error, the mean composite intrinsic thermal resistances, R_{Com} were determined to be R_{Com}=(0.760±0.036)×10^6 K/W, R_{Com}=(1.180±0.033)×10^6 K/W and R_{Com}=(2.36±0.041)×10^6 K/W for the P3HT NWs with 350 nm, 220 nm and 120 nm diameter, respectively.

From equation (2) and a low dispersion statistical study over 20 NWs, the local thermal conductivity of the composites was deduced to be $\lambda_{Com} = 1.89 \pm 0.08\ \mathrm{W/mK}$, $\lambda_{Com} = 1.18 \pm 0.06\ \mathrm{W/mK}$ and $\lambda_{Com} = 1.31 \pm 0.02\ \mathrm{W/mK}$, for composites made of P3HT NWs with 350nm, 220nm and 120nm diameters embedded in porous alumina matrix, respectively. It is important mentioning that these values are extremely useful, and relevant, as it constitutes the thermal conductivity values of possible functional devices.

Finally, the intrinsic NWs thermal conductivity is calculated using equation (5). In Table I the areal packing density of the NWs array evaluated from digital analysis of

SEM pictures of the samples top views, the thermal conductivity of the three different composites (considering it as a mixture of alumina and P3HT material), and the thermal conductivities of individual P3HT NWs with 350 nm, 220 nm and 120 nm diameters is shown. The validity of the effective medium theory to determine the thermal conductivity of individual NWs have been checked with 3D simulations of the different samples under the same experimental conditions as shown in Supplementary Information (S5).

The results shown in Table I clearly evidence the reduction of the thermal conductivity of individual P3HT NWs. For semicrystalline polymers, thermal conductivity is known to depend on both the degree of crystallinity and the orientation of their structural elements, i.e. molecules, aggregates, crystals, etc. [28] On the one hand, crystals show intrinsically higher conductivity than amorphous regions, in such a way that thermal conductivity of semicrystalline polymers is usually higher than that of amorphous polymers. On the other hand, orientation phenomenon leads to a large anisotropy in the thermal transport of semicrystalline polymers, that can be commonly understood considering that molecular chains in the crystallites are aligned in a certain direction, thus offering little thermal resistance along that direction. P3HT is known to be a semicrystalline polymer and thus, the consideration above should be taken into account when studying its thermal transport. Recently, Feng et al. have shown that thermal conductivity of P3HT does not depend significantly on density, which can be directly correlated to degree of crystallinity of the polymer [29]. They observed an increase of only 12 % of the thermal conductivity between P3HT films having density values around 1 g/ml (which according to Ro et al. corresponds to completely amorphous P3HT [30]) and those having values around 1.6 g/ml (highly crystalline P3HT). This low crystallinity dependence of the thermal conductivity in polymers having medium degrees of crystallinity, like P3HT (the degree of crystallinity of bulk P3HT has been proposed to be somewhat below 50 % [31]), has been suggested to be a consequence of the difference in elastic properties between amorphous and crystalline regions, which causes a high thermal boundary resistance at the many interfaces between amorphous regions and crystals[28].

In contrast, orientation phenomena are likely to modify strongly the thermal conductivity of semicrystalline polymers and to induce a large anisotropy as a function of the crystallographic directions. Piraux *et al.* [32] observed that the thermal conductivity of oriented polyacetylene films (another semicrystalline conjugated polymer) were 15-60 times higher than that of the non-oriented polyacetylene. Kiliam *et al.* [33] reported that the thermal diffusivity in stretched polyethylene was 50 times higher along the drawing direction than along the perpendicular direction. Moreover, this observation contrasts to the behavior of amorphous polyethylene, for which only a 2 fold increase was measured. This fact points out the special relevance of crystal orientation phenomena when dealing with semicrystalline polymers. Likewise, Feng et al. has recently reported a strong anisotropic thermal transport in P3HT films along the 3 spatial dimensions [10].

2D-nanoconfinement, like the one imposed by the cylindrical nanopores of AAO templates, frequently induces a preferential orientation of the confined polymer crystals [34] [35] . Thus, to elucidate whether changes in the orientation of P3HT crystals in the NWs may be at the origin of the reduction of their thermal conductivities, WAXS measurements were carried out for two different spatial directions, i.e. directions parallel and perpendicular to NW long axis. Note that, 2D patterns were collected in the direction perpendicular to NWs and then converted to one-dimensional scattering profiles by radial averaging along the azimuthal angle. All the samples showed diffraction rings in the perpendicular direction (not shown).

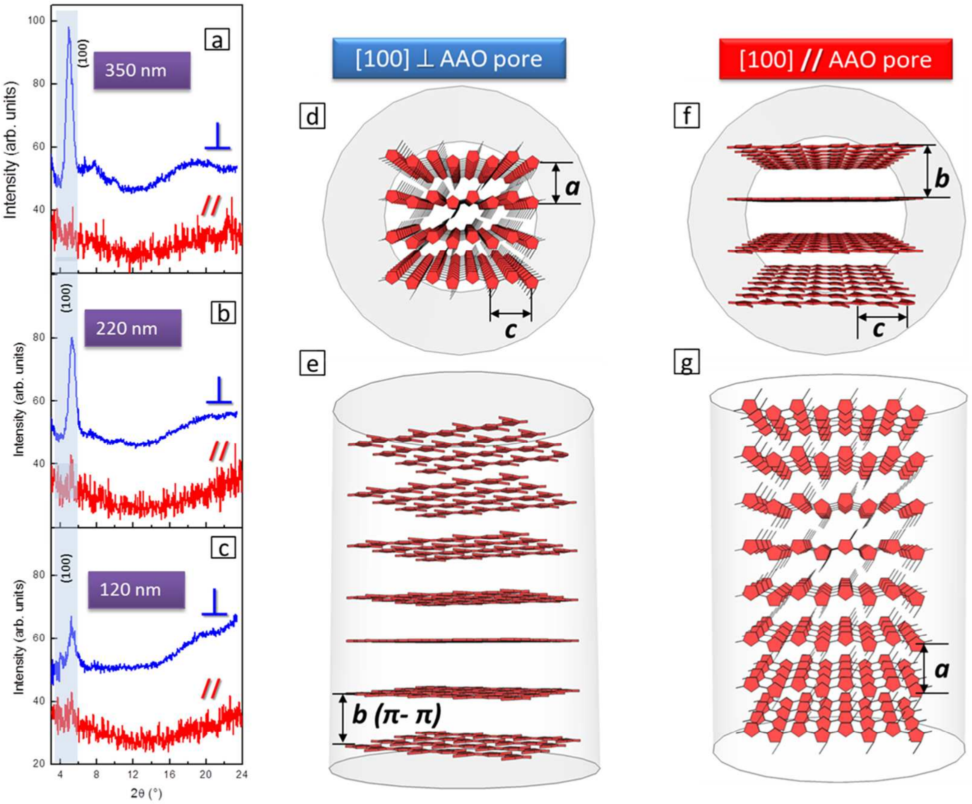

Figure 2. WAXS diffractograms of ensembles of P3HT NWs in which the wave vector, *Q,* was perpendicular to nanowires (lower red line with || symbol) and parallel to nanowires (upper blue line with ├ symbol) for (a) 350 nm, (b) 250 nm and (c) 120 nm NW arrays. Schematic illustrations of the 3 possible ideal spatial orientations of the P3HT crystallite within nanopores from up and transversal perspectives: (d and e) top and side view of the *b* axis of the crystal cell (π-π stacking direction) parallel to NW long axis which also corresponds to 100 perpendicular, and (f and g) top and side view of the *a* axis of the crystal cell ([100] growth direction) parallel to NW long axis.

In the experimental geometry in which the wave vector, *Q*, was perpendicular to NW long axis, the three samples (P3HT NWs of 350, 220 and 120 nm diameters) showed a diffraction maximum at 2θ = 5.2° corresponding to the stacking of the main chain/side-chain layered structure of the P3HT crystal along the *a* axis [36] [37] (Figure 2a, 2b and 2c). In general, in the three samples, crystals were preferentially oriented lying with their [100] crystallographic direction perpendicular to NW long axis and thus, the [010] direction (the π-π stacking direction) or the [001] directions lay preferentially parallel to the NW axis (ideally represented in Figure 2d,e). The most plausible orientation is the one in which crystals lay the π-π stacking direction parallel to nanowire long axis, as that orientation is the one fulfilling the Bridgeman mechanism [38]

[39 40] for orientations guided by kinetic aspects, as it has been usually observed in commodity polymers confined in nanopores [39 40]. Such mechanism dictates that the crystallographic direction with the fastest growth rate aligns parallel to the NW long axis. For P3HT crystal, π-π stacking direction is known to be the fastest growth direction[36 41], thus is expected to be parallel to NW long axis. The diffraction peak shows a decrease in intensity and a broadening upon reduction of the diameter of the nanowires from 350 to 120 nm. There are three main reasons for this: a) the porosity % of the alumina template is lower in the 120 nm (8%) than in 220 nm (25%) than in 350 nm (55%), so the amount of diffracting P3HT is the lowest in 120 nm. B) The crystal size is smaller while reducing the wire diameter, so the diffraction peaks become broader. And, c) some of the P3HT crystals may tilt under confinement.

The (100) diffraction for *Q* parallel to NWs long axis was absent in 350 nm nanowires, while weak (100) peaks become to be visible for 250 and 120 nm samples, being more intense in 120 nm nanowires. This means that as nanowire diameter is reduced, more and more crystals are tilt toward the [100] direction parallel to NWs axis. Note that in crystals with the [100] direction parallel to NWs axis, the [010] direction is almost perpendicular to the AAO pore walls. Since the [010] direction is that of the fastest growth, P3HT crystallites would tend to grow along that direction, but they impinge on the pore walls and die. This would lead these crystals to be considerably small, which would generate non-well-developed diffraction peaks when measuring in the geometry where *Q* is parallel to nanowire axis. This new configuration of the chain is ideally represented in Figure 2f,g).

To perform a semiquantitative analysis of the crystal orientation of P3HT NWs, an orientation parameter Γ, defined as $\Gamma = \gamma_{\perp} / 1.18\gamma_{\parallel}$, being $\gamma_{\perp}$ and $\gamma_{\parallel}$ the areas of the (100) peaks in direction perpendicular and parallel to the NW axis, respectively. The coefficient 1.18 was extracted from the ratio $\gamma_{\perp} / \gamma_{\parallel}$ of the bulk P3HT powder (Supporting information Figure S3), considering the fact that crystals must be isotropically oriented in that sample and thus Γ must be equal to unity (the P3HT was powdered in an agate mortar). In this way, Γ is closely related to the preferential orientation of the (100) planes in the NWs. Since $\Gamma > 1$ for the three samples, crystals laid with their [100] crystallographic direction preferentially perpendicular to the NW axis and thus, [010] and/or [001] directions were preferentially parallel to the NW axis (Figure 2e and 2f). As can be observed in Figure 3, Γ decreased as the pore diameter decreases, suggesting the presence of more and more crystals with [100] parallel to NWs, as ideally represented in Figure 2d. Note that although we cannot assure whether the extended polymer chain direction (*c* axis) or the π-π stacking direction (*b* axis) are parallel to NW long axis, both of them are expected to present little thermal resistance in analogous way to what occurs with electronic transport (the main electronic conduction in P3HT takes place along the thiophenic backbone and along the π-π stacking direction). This is because strong conjugated covalent bonds along the chain direction ([001] direction) and the compact π-π stacking (along the [010] direction) would facilitate the phonon transport along those crystallographic directions. In contrast, the [100] crystallographic direction is the one along which the alternation of layers of thiophenic chains and aliphatic chains take place. Thereby, insulating aliphatic regions separate the more conductive thiophenic layers, which may introduce additional thermal boundary resistances in the crystal structure along that direction. Furthermore, many authors maintain that medium size alkyl side chains, such as the hexyl groups of P3HT, keep disordered after the crystallization of tiophenic layers[42], which would increase further the thermal barriers at those regions. Therefore, we attribute the reduction of the thermal conductivity in P3HT NWs as reducing the diameter to the decreasing presence of crystals oriented with [010] crystallographic direction parallel to NWs. These results are qualitatively in accordance with the anisotropy of the thermal conductivity of oriented P3HT films found by Feng et al.[10] , as well as by other authors for non-conjugated polymers confined in nanopores [7].

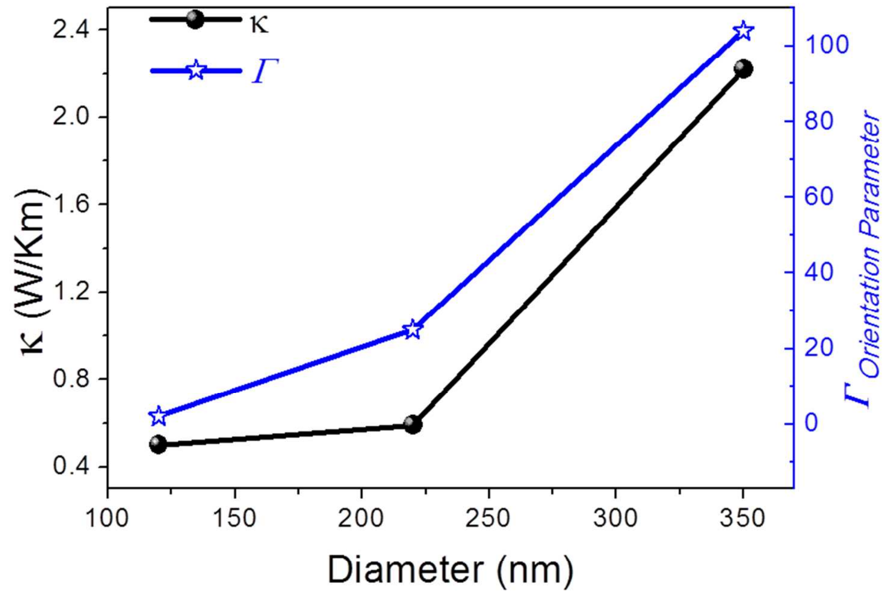

Figure 3. Plot of the thermal conductivity (black spheres) the orientation parameter, *Γ*, (blue stars) of P3HT NWs as a function of the NW diameter. $\Gamma = \gamma_{\perp} / 1.18\gamma_{\parallel}$, being $\gamma_{\perp}$ and $\gamma_{\parallel}$ the areas of the (100) peaks in direction perpendicular and parallel to the NWs axis, respectively. The coefficient 1.18 is extracted from the ratio $\gamma_{\perp} / \gamma_{\parallel}$ of the bulk P3HT.

Figure 3 shows that varying the diameter of the nanowire will lead to a reduction in its thermal conductivity. These nanowires could be used potentially in different application in thermal transport engineering because of choosing a particular diameter the changes in its thermal conductivity are appreciable. Therefore, the heat flow across a device could be controlled with a certain magnitude by selecting the appropriate P3HT diameter nanowire.

In summary, this work presents a correlation of the thermal conductivity of 1D semicrystalline polymer nanostructures with the orientation of their crystals. This involves a better understanding of the effects of size confinement in polymers and its correlation with their thermal transport. Particularly, P3HT nanowires of three different diameters were studied and a drastic reduction of their thermal conductivity was observed as reducing diameter. Such reduction is proposed to be consequence of an increasing presence of crystals oriented laying the [100] direction parallel to nanowire long axis. This analysis evidences the huge potential of nanoscale crystal engineering to modulate thermal transport along the NWs, which may establish the foundations of future nanostructured heat thermal transport engineering for different applications

Acknowledgments

Authors thank A. Nogales for WAXS measurements. M. M. R wants to acknowledge JAE-PreDoc for its financial support. And ERC 2008 Starting Grant "Nano- TEC" number 240497 and Nanotherm Consolider CSD-2010-00044 projects are acknowledged for financial support.

References

1. G. M. Whitesides, *Small*, 2005, **1**, 172-179.
2. M. Martín-González, O. Caballero-Calero and P. Diaz-Chao, *Renewable and Sustainable Energy Reviews*, 2013, **24**, 288-305.
3. M. Muñoz Rojo, O. Caballero Calero, A. F. Lopeandia, J. Rodriguez-Viejo and M. Martin-Gonzalez, *Nanoscale*, 2013, **5**, 11526-11544.
4. H. Ünlü and J. M. N. Horing, *Low Dimensional Semiconductor Structures*, Springer, Springer Heidelberg, 2013.
5. J. Martín, M. Krutyeva, M. Monkenbusch, A. Arbe, J. Allgaier, A. Radulescu, P. Falus, J. Maiz, C. Mijangos, J. Colmenero and D. Richter, *Physical Review Letters*, 2010, **104**, 197801.
6. S. Shen, A. Henry, J. Tong, R. Zheng and G. Chen, *Nat Nano*, 2010, **5**, 251-255.
7. B.-Y. Cao, Y.-W. Li, J. Kong, H. Chen, Y. Xu, K.-L. Yung and A. Cai, *Polymer*, 2011, **52**, 1711-1715.
8. J. Martin, M. Campoy-Quiles, A. Nogales, M. Garriga, M. I. Alonso, A. R. Goni and M. S. Martin-Gonzalez, *Soft Matter*, 2014.
9. C. Bounioux, P. Diaz-Chao, M. Campoy-Quiles, M. S. Martin-Gonzalez, A. R. Goni, R. Yerushalmi-Rozen and C. Muller, *Energy & Environmental Science*, 2013, **6**, 918-925.
10. X. Feng, G. Liu, S. Xu, H. Lin and X. Wang, *Polymer*, 2013, **54**, 1887-1895.
11. J. C. Duda, P. E. Hopkins, Y. Shen and M. C. Gupta, *Applied Physics Letters*, 2013, **102**, 251912.
12. L. A. Bottomley, *Analytical chemistry*, 1998, **70**, 425R-475R.
13. L. Shi, D. Li, C. Yu, W. Jang, D. Kim, Z. Yao, P. Kim and A. Majumdar, *Journal of heat transfer*, 2003, **125**, 881-888.
14. A. I. Persson, Y. K. Koh, D. G. Cahill, L. Samuelson and H. Linke, *Nano Letters*, 2009, **9**, 4484-4488.
15. K. G. Biswas, T. D. Sands, B. A. Cola and X. Xu, *Applied Physics Letters*, 2009, **94**, 223116-223113.
16. T. Borca-Tasciuc, D. A. Borca-Tasciuc and C. Gang, IEEE Transactions on Components and Packaging Technologies, 2007, **30**, 609.
17. Y. Zhang, C. Hapenciuc, E. Castillo, T. Borca Tasciuc, R. Mehta, C. Karthik and G. Ramanath, *Applied physics letters*, 2010, **96**, 062107.
18. E. Puyoo, S. Grauby, J.-M. Rampnoux, E. Rouviere and S. Dilhaire, *Review of Scientific Instruments*, 2010, **81**, 073701-073705.
19. E. Puyoo, S. Grauby, J.-M. Rampnoux, E. Rouviere and S. Dilhaire, *Journal of Applied Physics*, 2011, **109**, 024302-024309.
20. M. Muñoz-Rojo, S. Grauby, J. M. Rampnoux, O. Caballero-Calero, M. Martin-Gonzalez and S. Dilhaire, *Journal of Applied Physics*, 2013, **113**, 054308-054307.
21. S. Grauby, E. Puyoo, J.-M. Rampnoux, E. Rouvière and S. Dilhaire, *The Journal of Physical Chemistry C*, 2013, **117**, 9025-9034.
22. S. Lefèvre, S. Volz and P.-O. Chapuis, *International Journal of Heat and Mass Transfer*, 2006, **49**, 251-258.
23. J. Martín and M. Martín González, *Nanoscale*, 2012, **4**, 5608.
24. J. Martín, C. V. Manzano and M. Martín-González, *Microporous and Mesoporous Materials*, 2012, **151**, 311-316.
25. J. Martín, A. Nogales and M. Martín-González, *Macromolecules*, 2013, **46**, 1477-1483.
26. M. Hinz, *Applied physics letters*, 2008, **92**, 043122-043122-043123.
27. R. Prasher, *Nano Letters*, 2005, **5**, 2155-2159.
28. C. L. Choy, *Polymer*, 1977, **18**, 984-1004.
29. X. Feng and X. Wang, *Thin Solid Films*, 2011, **519**, 5700-5705.

30. H. W. Ro, B. Akgun, B. T. O'Connor, M. Hammond, R. J. Kline, C. R. Snyder, S. K. Satija, A. L. Ayzner, M. F. Toney, C. L. Soles and D. M. DeLongchamp, *Macromolecules*, 2012, **45**, 6587-6599.
31. Z. Wu, A. Petzold, T. Henze, T. Thurn-Albrecht, R. H. Lohwasser, M. Sommer and M. Thelakkat, *Macromolecules*, 2010, **43**, 4646-4653.
32. L. Piraux, M. Kinany-Alaoui, J. P. Issi, D. Begin and D. Billaud, *Solid State Communications*, 1989, **70**, 427-429.
33. H. G. Kilian and M. Pietralla, *Polymer*, 1978, **19**, 664-672.
34. J. Maiz, C. Martin and Mijangos, *Langmuir*, 2012, **28**, 12296-12303.
35. J. Martín, A. Martín, C. Nogales and Mijangos, *Macromolecules*, 2013, **46**, 7415-7422.
36. J. A. Lim, F. Liu, S. Ferdous, M. Muthukumar and A. L. Briseno, *Materials Today*, 2010, **13**, 14-24.
37. T. J. Prosa, M. J. Winokur, J. Moulton, P. Smith and A. J. Heeger, *Macromolecules*, 1992, **25**, 4364-4372.
38. P. W. Bridgman, *Proceedings of the American Academy of Arts and Sciences*, 1925, **60**, 306.
39. J. Martín, J. Maiz, J. Sacristan and C. Mijangos, *Polymer*, 2012, **53**, 1149-1166.
40. M. Steinhart, *Advances in Polymer Science*, 2008, **220**, 123-187.
41. M. Brinkmann, *Journal of Polymer Science Part B: Polymer Physics*, 2011, **49**, 1218-1233.
42. M. C. Gurau, D. M. Delongchamp, B. M. Vogel, E. K. Lin, D. A. Fischer, S. Sambasivan and L. J. Richter, *Langmuir*, 2006, **23**, 834-842.